IET Microwaves, Antennas & Propagation

The Institution of Engineering and Technology WILEY

ORIGINAL RESEARCH

Near-ground propagation in automotive radar and communication obstructed deployments: Measurements and modelling

Dmitrii Solomitckii[1] | **Vasilii Semkin[2]** | **Matias Turunen[1]** | **Markus Allén[1]** | **Mikko Valkama[1]**

[1]Faculty of Information Technology and Communication Sciences, Electrical Engineering Unit, Tampere University, Tampere, Finland

[2]VTT Technical Research Centre of Finland Ltd., Espoo, Finland

Correspondence

Dmitrii Solomitckii, Faculty of Information Technology and Communication Sciences, Electrical Engineering Unit, Tampere University, FI-33101, Tampere, Finland.
Email: dmitrii.solomitckii@tuni.fi

Abstract

Wireless communication and radars will play a crucial role for autonomous vehicles in the nearest future. However, the blockage caused by surrounding cars can degrade communication performance, while automotive radars are never aimed to operate in such conditions. Therefore, in this paper, the authors propose the concept of near-ground propagation, reducing the blockage effect in the road traffic conditions. Specifically, the radio waves may freely propagate under the blocking car's bottom if the antennas are placed as low as possible to the road. Based on the measured and modelled results presented in the paper, it may be claimed that near-ground communication and radar sensing are feasible and may combat even heavily obstructed cases. Nevertheless, some challenges associated with antenna locations were encountered. For example, it was discovered that antenna height at 0.5 m acts less effectively against blockage than at 0.3 m. Next, the 27 dB excess loss at the 0.5 m antenna height in the radar deployment is larger than 17 dB at 0.3 m. In its turn, the higher ground clearance of the blocking vehicle positively affects the near-ground performance. Additionally, the signal propagation at the grazing angle crucially reduces the relevant losses.

KEYWORDS

automotive communication, automotive radar, blockage, millimeter-wave, near-ground

1 | INTRODUCTION

The emergence of autonomous vehicles and road infrastructure opens a new chapter in the wireless communication and sensing topic for the automotive industry. According to Ref. [1], the autonomous (driverless) car market was valued at 20.97 billion USD in 2020, with an expectation to rise to 61.93 billion USD in the next 5 years. Following such great perspectives, nowadays, many companies are actively involved in research and development to find a niche in this segment. As a result, we may regularly observe new prototypes with a full or partial level of autonomy. For example, some car brands already offer commercial models with an advanced autopilot capability, including driving along the curved road, guided by marking

lines and signs and slowing down in case of potential danger. However, in such partially autonomous vehicles, the driver is still irreplaceable here since extra-human visual control is required [2]. Hence, wireless technologies do not play a vital role here but are bordered by driving assistance, safety and comfort enhancements. On the contrary, fully autonomous vehicles (e.g. Waymo, Zoox, Apple etc.) may raise the importance of wireless technologies as they determine the possibility to exploit such fully autonomous vehicles safely and reliably on public roads to a large extent. In other words, the operation of such vehicles is impossible without deploying wireless technologies and related infrastructure around them.

In addition to the R&D, the standardising and documenting work on the automotive wireless technologies is

underway. For example, the Third Generation Partnership Project (3GPP) proposed combining LTE and 5G New Radio (NR) to achieve the best performance [3] in vehicular scenarios. In this standard, communication partially occurs at millimetre-wave (mmWave and at microwave) frequencies with antennas installed in the bumper/radiator area. On the other hand, a distinct wireless technology, radar sensing, is well described and classified in recommendations from the International Telecommunication Union (ITU) [4]. Additionally, because of similar nature as well as cost and spectrum benefits, converging the radar and communication parts in a single hardware unit [5] might be a logical step forward. Nevertheless, radar and communication follow their own life journey and do not intersect in any standardisation documents so far; there are many open issues.

Apparently, line-of-sight (LOS) is a working condition typically required for vehicular communication and radar sensing. However, the appearance of a car without or broken communication equipment in dense traffic may turn the LOS into the obstructed LOS (OLOS) scenario, where special methods should be applied to connect blocked vehicles. For example, the link might be rebuilt by the car relaying [6] method or employing the infrastructure roadside units (RSU) as intermediate nodes [7]. However, underdeveloped road infrastructure or traffic jams may drop the performance of the suggested schemes. Hence, the following logically correct issue is raised: *Is there a way to keep the vehicles connected in the OLOS conditions without infrastructure assistance or relaying?* In this paper, a solution to install the communicating antenna as close as possible to the road, enabling signal propagation between the obstructing vehicle and pavement (waveguide-like propagation), is suggested. This effect may keep the vehicles connected and expand the existing radar capabilities even in an OLOS scenario. Such phenomenon is called *near-ground propagation* in vehicular deployment. This topic was partly presented earlier in Ref. [8]. This paper extends the original work by introducing a detailed analysis and deterministic site-specific modelling.

In general, near-ground propagation has already been covered in the literature earlier mainly for agricultural or forest scenarios [9–13]. Specifically, in Ref. [10], the authors presented a methodology to model the near-ground short-range propagation loss in the forest areas. The attenuation of the received power was measured for both transmitter (Tx) and receiver (Rx) antennas at 0.2 and 0.4 m heights, respectively. Later, in Ref. [9, 11], the same group of authors developed the near-ground narrowband radio channel model for agricultural wireless sensor networks. A pretty similar problem is explored in Ref. [12], where the continuous-wave measurements at 917.5 MHz in a forest terrain with a focus on path-loss in a device-to-device communication scenario were carried out in a few kilometre ranges extending at 1.5, 2.5, and 3.5 m height. Finally, in Ref. [13], 300 and 1900 MHz narrowband and wideband channel measurement results are presented for near-ground propagation. As a part of it, the antenna height, radiation patterns and foliage effects were investigated.

Besides agriculture and forest use cases, near-ground propagation can be found in some other applications. For example, in Ref. [14], the functionality of a military man-portable near-ground radio transceiver is introduced. The results of this study show a significant deviation of signal strength when the position of a soldier is changed. Further, in Ref. [15], based on analysis of the propagation environment and received ultrawideband signal in outdoor near-ground environments, the main path-loss models are considered. Also, in Ref. [16], near-ground localisation is explored. In the research study, the antenna height-dependent time of arrival error model is developed. Another quite exciting outcome was obtained in Ref. [17], where an efficient two-segment ultrawideband radio channel model is introduced in very near-ground environments at height 0–20 cm. Later, the model was validated by measurement at 4.3 GHz with a bandwidth of 1 GHz. Finally, the results in Ref. [18–20] demonstrate the measurement and modelling results of the near-ground propagation without focussing on any application.

Nonetheless, all these earlier studies on near-ground propagation did not consider any vehicular deployments. Therefore, we aim to fill this gap by introducing the near-ground propagation in the OLOS vehicular deployment. Specifically, the goals and contributions of this paper can be stated as follows:

1. To introduce the measured results of radar and communication parts obtained by the authors in the OLOS scenario with a near-ground propagation effect.
2. To propose and validate the method for practical modelling of the OLOS scenario with a near-ground propagation effect.
3. To perform the sensitivity analysis of the OLOS scenario with a near-ground propagation.

The paper is organised as follows. First, the antenna height requirement is determined for the realisation of near-ground vehicular applications in Section 2. Next, the deployment of interest and the measurement equipment are introduced in Section 3. Similar, but virtual deployment and modelling methods are described in Section 4. The measurement, modelling and sensitivity analysis results are provided in Section 5. Finally, the conclusions and discussions are presented in Section 6.

2 | THE NEAR-GROUND DEFINITION IN VEHICULAR DEPLOYMENTS

As it was mentioned in Section 1, the antenna should be attached as low as possible to the road surface in order to create the near-ground propagation effect. Moreover, the number of near-ground applications with distinguishing heights have been considered. Hence, only a use case defines how close the antennas should be to the ground. This section will define the near-ground height for vehicular application

based on geometrical measurements, observations, and in-depth literature review.

Based on the empirical studies (listed in Table 1), typical ground clearance[1] a of road vehicles varies within a relatively small range of up to 20 ± 10 cm with respect to, for instance, length or height [21]. Exotic off-road or sport cars are rear and are not considered in this work. Based on the under-car geometry (subfigure in Figure 1a), the immediate intuitive intention to place the antenna at some constructive elements (protruding parts of axles, gearbox, driveshaft etc.) looks unrealistic for the following reasons. First, the location of the elements varies from model to model. Therefore, every vehicle should be considered individually, which may complicate the development of a common standard. Second, the constructive elements may be a subject to stress, vibrations or dust affecting the near-ground propagation performance. Following this and the data in Table 1, the suitable area for the near-ground antenna placement was defined in *the lowest point of the car bumper* at height 0.3 m for cars and 0.5 m for trucks. These two reference values will be used further thoroughly in our study. Also, front and rear bumper lower heights b and c listed in Table 1 and shown in Figure 1a will be considered in Section 5 as additional parameters, affecting the signal propagation.

3 | MEASUREMENT METHODOLOGY

First, the measurements were performed to prove the concept of near-ground propagation in the OLOS deployment. The measurement scenario and the utilised mmWave setup are described below.

3.1 | Measurement scenario

The measurements were carried out on the territory of Tampere University with the mmWave setup developed at the Faculty of Information Technology and Communication Sciences. In this measurement campaign, two deployments were considered: (i) communication (shown in Figure 1a) and (ii) radar (presented in Figure 2a). In the first scenario, two abstract vehicles communicate through antennas (red and black triangles in Figure 1a) installed on the lowest points of their bumpers. The signal blocking vehicle Kia Ceed (the white car in Figure 1a) is located between the antennas to form the required OLOS scenario. The antennas height H as well as distances D_1 and D_2 are taken as variables to mimic different vehicle types and road conditions. Specifically, two heights (H) of 0.3 and 0.5 m refer to the lowest bumper point of a passenger car and a truck (as defined in Section 2), while the $D_1 = D_2 = 1$–10 m characterise the varying vehicular density

TABLE 1 Measured dimensions of some road vehicles

N	Model	a, m	b, m	c, m
1	Kia Ceed (2015)	0.14	0.18	0.27
2	Saab 9-3 Aero (2002)	0.13	0.16	0.23
3	Audi A4 (2018)	0.13	0.17	0.26
4	Mini Cooper (2010)	0.15	0.19	0.24
5	Skoda Octavia (2018)	0.16	0.20	0.27
6	Mercedes-Benz ML (2011)	0.20	0.28	0.35
7	Toyota Land Cruiser (2012)	0.23	0.3	0.38
8	MAN (not identified)	0.25	0.50	0.45
9	SISU (not identified)	0.27	0.45	0.40

on the road: short D_1 and D_2 relate to traffic jam, while large ones describe sparse road density.

The second measurement scenario focusses on the automotive radar operation in the OLOS condition. In such a scenario, the presence of the near-ground propagation potentially may give extra awareness about the front and rear dynamics in the traffic flow, using the backscattering from the vehicles in the traffic queue. Therefore, to imitate this use-case, the radar transceiver, represented by collocated Tx and Rx antennas, is engaged in the scenario. Furthermore, in addition to the blocking Kia Ceed, Saab 9-3 Aero (black car in Figure 2b) was appended to imitate the mobility in the traffic queue. The distance D_3 had a discrete range from 1 to 5 m with 1 m step, while D_4 dynamically varied from 1 to 15 m when the vehicle drove. Values of H are similar to the communication scenario. First, the mmWave setup (transceiver) is installed at a certain distance D_3 to the blocking vehicle. Then, by the command of the equipment operator, Saab 9-3 Aero starts moving, and D_4 begins increasing. The measurements are performed while the car is driving. The requirement for smooth linear acceleration was determined to avoid significant deviation of the captured data. The maximal speed 2 m/s was chosen for safety reasons.

3.2 | Measurement equipment

Radar and communication setups were assembled and utilised for the measurement of the radar and communication deployments explained in Section 3.1. The transmitting part was common while receiving parts are individual for each setup. The total received power P_{tot}^{com} and the backscattering P_{bsc}^{rad} power were selected as measuring values of interest. It is noteworthy that the antenna radiation patterns were measured in the anechoic chamber at Aalto University. The measurement results are shown in Figure 3.

Radar/Communication Tx: The NI PXIe-5840 vector signal transceiver (VST) generated the modulated OFDM signal with 200 MHz bandwidth and 60 kHz subcarrier at an intermediate frequency (IF) of 3.5 GHz. The Tx Pasternack PE9851A-20 horn antenna was installed on the tripods at the

---

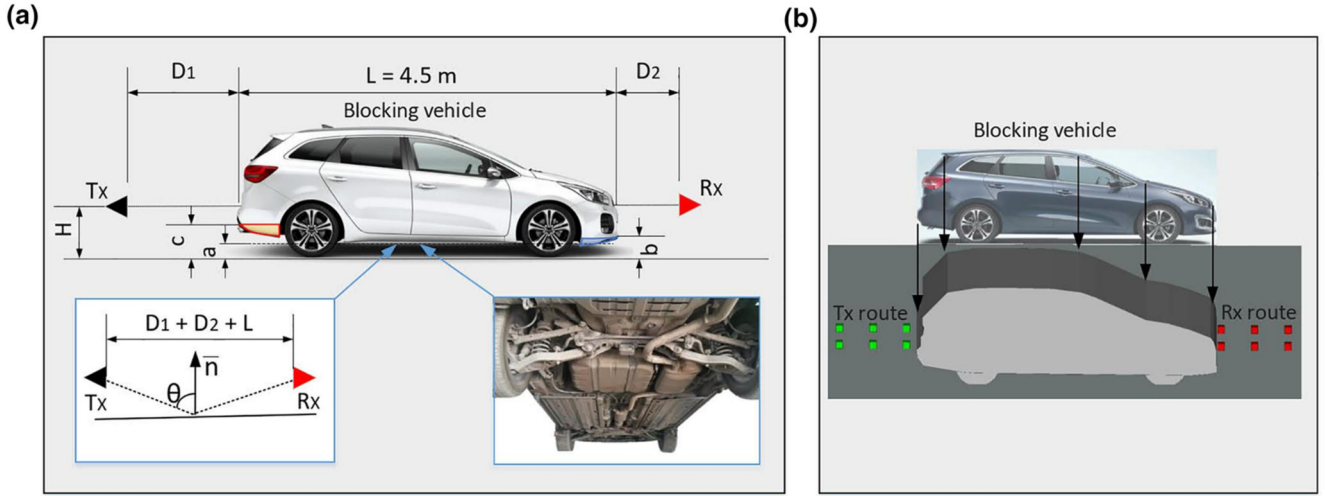[1]The distance between the road pavement and the lowest point of the central part of the car.

FIGURE 1 (a) Deployment for the measurement of the total received power in communication part. (b) The virtual modelling deployment for communication part built in Wireless Insite
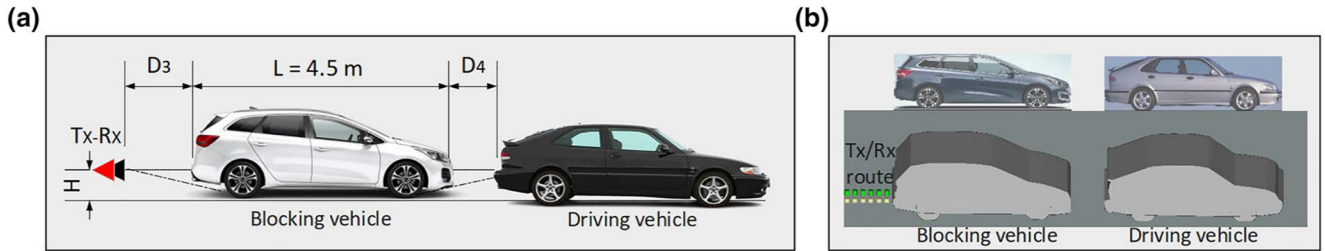

FIGURE 2 (a) Deployment for the measurement of the backscattering power in the radar part. (b) The virtual modelling deployment for the radar part built in Wireless Insite
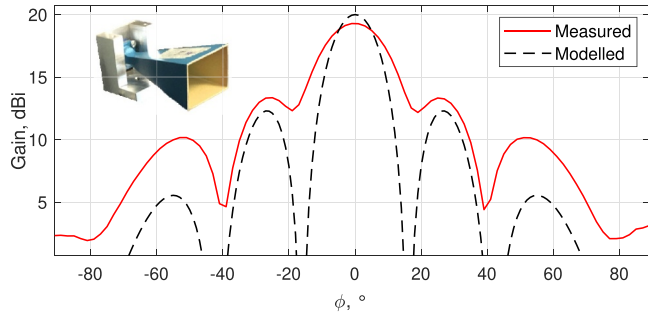

FIGURE 3 Co-polar measurement and modelling of the radiation pattern of the horn antenna PE9851A-20

height of H. The transmitted power was 10 dBm. Finally, the Keysight N5183B signal generator is operated as the local oscillator with external mixers to up-convert the IF signal to 27.7 GHz.

Communication Rx: The 27.7 GHz spectrum analyser (SA) Anritsu MS2760A was employed to measure $P_{\text{tot}}^{\text{com}}$ at the resolution bandwidth of 100 kHz and measurement bandwidth of 200 MHz. In these conditions, it had the noise level of −55.5 dBm. The PE9851A-20 horn antenna with 20 dBi gain and the 17° half-power beamwidth were attached to the SA by a cable with the 8 dB insertion loss.

Radar Rx: The NI PXIe-5840 VST received $P_{\text{bsc}}^{\text{rad}}$ at an IF of 3.5 GHz through similar Pasternack antennas installed on the tripods at the height of H. The radar collocated antennas were spatially separated by 0.1 m. The Keysight N5183B signal generator used as down-converter. For all the measurements, the duration was constant: 10 ms. Finally, sub-carrier-domain processing algorithms were developed [22] to post process the measurement results.

4 | MODELLING

The ray tracing (RT) techniques in Wireless Insite [23] (WI) software was selected for simulation of near-ground propagation in the OLOS conditions. There are couple of reasons for choosing this. First, the multipath representation exposes a fairly intuitive picture of the propagation mechanisms happening between the car bottom and ground. For example, this approach enables the classification of the dominant and weak effects under the vehicle. Second, the sizes of the vehicle and the ground are large compared to that of the wavelength ($\lambda \approx 1$ cm), suggesting ideal conditions for utilisation of geometrical optics (GO) and uniform theory of diffraction (UTD) [24] of the RT. Alternatively, full-wave methods are inefficient for such cases since, for instance, triangulation

would require much memory and an unreasonably long computational time. Third, the employment of the radar theory for the radar deployment explained in Section 1 looks quite controversial due to the large dimensions of the ground and vehicle. This fact contradicts to the basics, where the object–radar distance should be infinitely large to turn the detecting object into a point scatterer [25]. Moreover, the selection of WI is validated in Section 5.3 by the LOS calibrating measurements, where the backscattering from the car is well approximated by the Friis equation (FE; see Figure 5a,b).

A simplified 3D model of Kia Ceed was created to simulate the OLOS near-ground scenario in the Wireless Insite environment for the communication part (shown in Figure 1b). First, an image of the original Kia Ceed was uploaded, and then, using the built-in shape editor, a 2D contour was outlined and extruded to a 3D model. Apparently, due to the near-ground propagation, the contour of the blocking vehicle (Kia Ceed) should be as accurate as possible (i.e. geometry and overhangs of bumpers, ground clearance etc.), while some other details might be neglected or simplified. For example, it was speculated that the car model is completely PEC, which is a fairly rough approximation since the bumper, for instance, is hollow, made of plastic, and has a lot of metallic elements and wires behind it. However, it is pretty challenging to reproduce all the internals for any car, and hence it was suggested to nullify their contribution. Also, the bottom of the virtual vehicle is shortened to entirely flat for the same reasons. Nevertheless, the obtained accuracy of the modelling results in Section 4 was reasonable even with these simplifications.

The simulated radar deployment is shown in Figure 2b, where another simplified 3D model of Saab 9-3 was added. The Rx-route is collocated with the Tx-route, representing the Tx-/Rx-route in the rear side of the blocking vehicle. Special batch functions were realised to perform the multi-frame dynamics of the Saab model; its position may change by 1 m forward in each frame. For each position, the signals on the transceivers were calculated in WI and were stored. This total number of discrete positions is 10, that is, the maximal distance is 10 m.

The PE9851A-20 antenna was utilised at the Tx and Rx sides. The measured and the calculated patterns (with Wireless Insite) are presented in Figure 3. The discrepancy between the measured and simulated antenna patterns do not significantly affect the final result because of coaxiality between the antennas and the absence of any side objects. The maximum realised gain of 19.2 dBi was obtained in the modelling, while the gain of 20 dBi was measured. Despite the relatively low antenna location, the ground impact on the main lobe, thoroughly utilised in the manuscript, is not significant. Specifically, at $H = 0.3$ m and HPBW = 17°, the main beam starts interacting with the ground at 0.98 m, whereas the far-field zone begins from 0.47 m.

The utilised simulation parameters are listed in Table 2. The RT built-in models are well described in Ref. [27] and will not be highlighted in this paper. However, an in-depth analysis of the reflected signal in the context of near-ground propagation will be performed in Section 5. Specifically, the equation describing the single-reflecting signal might be written as follows:

TABLE 2 Modelling parameters

N	Model	Value	Notes
1	ϵ_c of road	4.4 - j0.2	[26]
2	σ_b of road, m	0, 0.001	
3	Material of car(-s)	PEC	From WI database
4	# Of refl., pcs	1–3	
5	# Of trans., pcs	0	
6	# Of diffr., pcs	1	
7	# Of multipaths, pcs	50	per each Tx-Rx pair

$$E_r = \begin{bmatrix} E_i^{\|} \\ E_i^{\perp} \end{bmatrix} \cdot \begin{bmatrix} R_{\|} & 0 \\ 0 & R_{\perp} \end{bmatrix} \cdot \rho_s \cdot \frac{e^{-jks'}}{s'}, \quad (1)$$

where s' the Tx–Rx distance, $E_i^{\|}$ and $E_i^{\perp}$ are incident electrical fields. Further, $R_{\|}$ and $R_{\perp}$ are Fresnel reflection coefficients for horizontal and vertical polarisations, which are defined as follows:

$$R_{\|} = \frac{-\epsilon_c \cos(\theta) + \sqrt{\epsilon_c - \sin(\theta)^2}}{\epsilon_c \cos(\theta) + \sqrt{\epsilon_c - \sin(\theta)^2}} \quad (2)$$

$$R_{\perp} = \frac{\cos(\theta) - \sqrt{\epsilon_c - \sin(\theta)^2}}{\cos(\theta) + \sqrt{\epsilon_c - \sin(\theta)^2}} \quad (3)$$

At the same time, the signal reflecting from a rough plane undergoes additional attenuation, specified by the roughness coefficient ρ_s. The attenuation rate depends on the angle of incidence θ (see explanation in Figure 1a), the wavelength λ, and the size of the irregularities σ_s as follows:

$$\rho_s = \exp\left(-\frac{1}{2} \left(\frac{4\pi\sigma_b \cos(\theta)}{\lambda} \right)^2 \right). \quad (4)$$

From the mathematical point of view, a distinctive feature of Equations (2)–(4) is approaching to unity at $\theta \to 90°$. It means that roughness and dielectric parameters of the road become negligible at grazing angles, enabling the lossless reflecting field, in theory. This positive feature will be discussed in the next sections.

5 | RESULTS

5.1 | Total received power in the OLOS near-ground vehicular deployment

First, about hundreds measurements of the P_{tot}^{com} at the distance ranges $D_1 = 1$–10 m and $D_2 = 1$–10 m at $H = 0.3$ and 0.5 m were carried out in the communication scenario,

described in Section 3.1. In these measurements, the discrete values of D_1 and D_2 were varied with step $\Delta_{meas.} = 1$ m. For each discrete distance of D_1, 10 power samples were captured along the range D_2 from 0 to 10 m. Later, the measured data was stored and tabulated. The results of these hundreds measurements at $H = 0.3$ m were collected in a single plot and shown in Figure 4. In this paper, the data at $H = 0.5$ m is not depicted similar to Figure 4, since it highly correlates with $H = 0.3$ m and does not discover any new finding. Therefore, on the basis of Figure 4, the following conclusions can be obtained. At shortest D_1 or D_2 the P_{tot}^{com} approaches to the noise level because of the strong blockage effect. Nevertheless, the level of the blockage is different near the front and the rear bumper because of, probably, distinguishing bumper geometry. It can be recognised by depth and width of the blue region along D_1 or D_2. Meanwhile, the maximum value of the total received power was identified at 2–3 m of D_1 or D_2. At these distance ranges, the blockage effect is negligible, as a predicted priori. These preliminary results are quite encouraging, and therefore additional measurements are required to deepen the observed relationships.

It is evident that the most interesting region for further investigation is the transition from strong (blue colour in Figure 4) to weak (deep red colour in Figure 4) obstruction. These distances are $D_1 = 1$–4 m and $D_2 = 1$–4 m. Additionally, step $\Delta_{meas.}$ was reduced down to 0.2 m to improve the measurement accuracy. The results of these additional 225 (15 for D_1 and 15 for D_2) measurements at $H = 0.3$ m are illustrated in the small Figure 4. Based on this, the next set of outcomes might be delivered. Indeed, the symmetry of the blue regions of $D_1 = D_2$ in Figure 4 was not reached again (as in $\Delta_{meas.} = 1.0$ m). On the contrary, the blue-to-red transition region of interest becomes less sharp: some intermediate colours appeared in the small figure. It is notable in Figure 4 and Table 1 that the front bumper is more ground-close than the rear one. Therefore, it blocks the near-ground signal stronger, which affects the difference of the blue zones along D_1 and D_2. Moreover, based on Table 1, the $c > b$ rule is typically satisfied for all the listed and, probably, most of the existing vehicles. Meanwhile, the position of data points, referencing
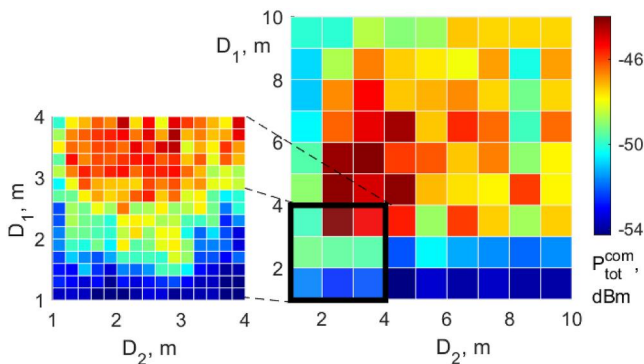
the maximum total received power in the communication scenario, is localised in the range of 2–4 m. To explain this phenomenon, two-dimensional plots, comparing the P_{tot}^{com} with the theoretical FE as a function of total distance between antennas $D_1 + D_2 + L$ and H were derived from the originally measured data. Specifically, Figure 5a,b relate to $H = 0.3$ m and $H = 0.5$ m, accordingly. In both graphs, the measured values are denoted as red circles, while the black solid line represents FE. The introduced made-by-sight dashed lines A and B bound the measured data and will help to explain the observed relationships in the following sections. These lines are shown for better visualisation.

When antennas are next to the blocking car (i.e. $D_1 + D_2 + L = 7$ m in Figure 5a and $D_1 + D_2 + L = 10$ m in Figure 5b), the signal is strongly obstructed, and contribution to the P_{tot}^{com} is almost zero. As soon as $D_1 + D_2 + L$ starts gradually increasing, the P_{tot}^{com} begins proportionally raising
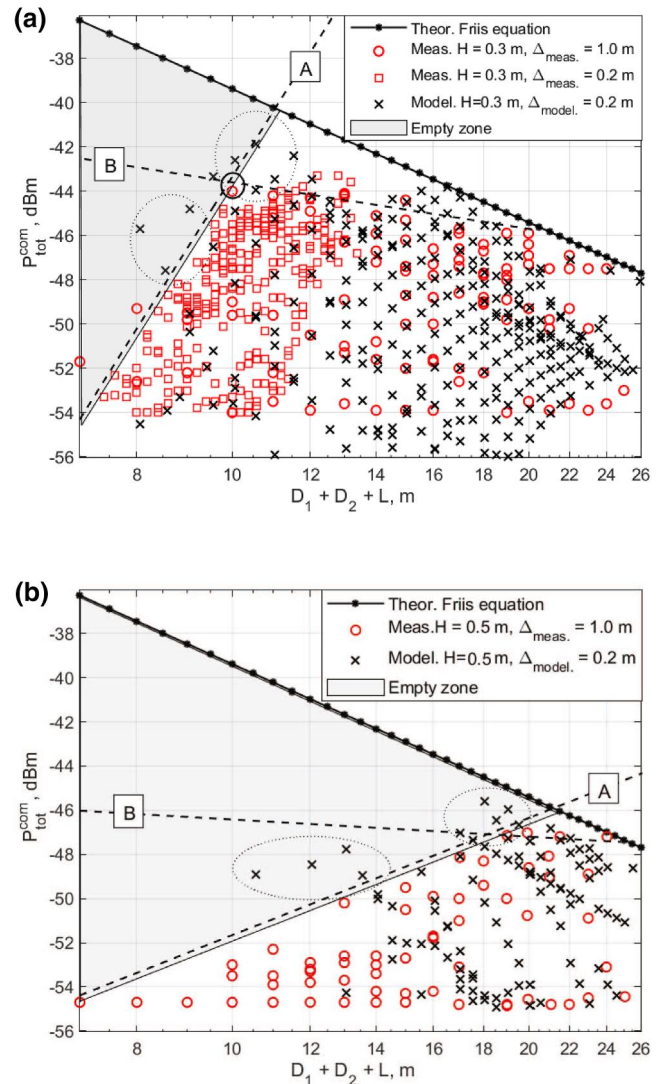

FIGURE 5 Measured (red circles) and modelled (black crosses) total received power as a function of $D_1 + D_2 + L$ at (a) $H = 0.3$ m and (b) at $H = 0.5$ m

FIGURE 4 Measured total received power as a function of D_1 and D_2 at $H = 0.3$ m. The small figure precises the measured data in the range $D_1 = D_2 = 1$–4 m

along the dashed line A as well, due to the diminishing role of the blockage effect. On the contrary, the growth of the total received power along the dashed line A goes slower for heights $H = 0.5$ m. This observation is quite intuitive: the higher H, the greater distances D_1 and D_2 are needed to detect the first near-ground multipath.

The maximum level (circled point) of $P_{\text{tot}}^{\text{com}} = -43$ dBm at $H = 0.3$ m and $P_{\text{tot}}^{\text{com}} = -47$ dBm at $H = 0.5$ m is associated with the full termination of the blockage and the appearance of a first-order reflection from the ground. After the peak is reached, the measured data points start to be distributed along the dashed line B, distanced to FE because of reflection losses. Further, as the distance $D_1 + D_2 + L$ increases, the angle θ (see Figure 1a) expands proportionally, which, in turn, causes the reflection (Equations (2) and (3)) and scattering coefficients (Equation (4)) to approach unity (see Section 4). Consequently, at relatively large distances $D_1 + D_2 + L$, due to the presence of grazing angle, the losses tend to be zero either. Following to our measurements, the near-ground lossless transmission appears at 18 m for $H = 0.3$ m and 22 m for $H = 0.5$ m, accordingly. Starting from these distances, the received power converges with the FE. Additionally, it should be emphasised that the near-ground propagation happens at some threshold distance. For $H = 0.3$ m, the threshold distance is about 8 m, which corresponds to $D_1 = D_2 = 1.7$ m, while at $H = 0.5$ m, the first multipath component might be already captured by Rx at $D_1 = D_2 = 2.7$ m.

Finally, the simulated Wireless Insite data is introduced in Figure 5a,b as black crosses. The simulation settings listed in Table 2 with a single reflection were utilised to obtain these figures. In general, the behaviour of the received power $P_{\text{tot}}^{\text{com}}$ corresponds to the measured values. However, it can be seen that some circled data points distributed in the range of 8–10 m, 10–12 m in Figure 5a and 10–14 m, 16–22 m in Figure 5b exceed the line A. There might be a couple of reasons for this. Probably, this may happen due to the limited accuracy of the 3D model or utilised GO and UTD methods. Misalignment between the measured and modelled results in vehicular deployments may easily be 4 dB or even higher [28]. However, investigation of individual multipath components to determine the source of the divergence in such an unfavourable scenario is, in principle, quite difficult. The main reason for this is the limited bandwidth of the measuring equipment to resolve the captured bunch of multipath components with minimal time- (<0.5 ns) and angle-of-arrival (few degrees) differences caused by the grazing angle. Therefore, the point-to-point matching between the measurements and modelling data is quite challenging. This negative factor, unfortunately, induced to compare the data distribution behaviour (in Figure 5a,b) rather than point-to-point multipath matching.

5.2 | Backscattering power in the OLOS near-ground vehicular deployment

The next step is analysing the backscattering power $P_{\text{bsc}}^{\text{rad}}$, returning from the driving vehicle (Saab 9-3 Aero in Figure 2a)

under the blocking car (Kia Ceed). At that end, the distribution of $P_{\text{bsc}}^{\text{rad}}$ as a function of speed V and total distance $D_3 + D_4 + L$ was collected and stored. Specifically, Figure 6a exhibits the picture of all the 15 overlaying measurement snapshots (in the figure, only #1 and #15 are denoted) per single driving. These backscattering snapshots are distributed along the dynamic trajectory of Saab (black piece-wise solid line). The shape of the route is divided into acceleration zone (range 10–15 m) and the constant speed regime (range 15–24 m). Unfortunately, the desirable constant speed driving was not reached due to the reasons explained later in this section. Finally, the large red blob in the bottom is a high-power reflection from the blocking vehicle (in this case, Kia Ceed, Figure 2a).

For each of the discrete D_3 distances, three drivings were completed with the Saab car and measurements were collected to get statistical data for further processing. As an example, three measured snapshots of the backscattering power at similar $D_3 = 5$ m and $D_3 + D_4 + L \approx 16$ m are depicted in Figure 6b. In first two subfigures, the position of the snapshots is almost identical, while the third one is biased by $\delta = 1.3$ m along the Y-axes. The main reason for this is the varying driving speed of Saab, caused by (i) limited driver's ability to operate the gas pedal and (ii) measurement delays. The first effect is explicitly demonstrated in Figure 6a, where keeping the constant speed in the eponymous zone of the driving trajectory was not fulfiled. The latter reason is related to the sub-second delays caused by the setup operator reaction and the measuring hardware processes.

Similarly to the communication part described in Figure 5a,b, the backscattering power $P_{\text{bsc}}^{\text{rad}}$ as a function of $D_3 + D_4 + L$ and H is plotted in Figure 7a,b. However, unlike the communication part, additional LOS measurements without the blocking vehicle were completed in the radar deployment. The base goal of this is similar to the communication part: to evaluate the near-ground-related losses. Nonetheless, additionally, it was done to clarify the issue which propagation formula the backscattering signal should be described by FE or Radar range equation (RRE). Typically, the latter is commonly applied to any radar scenarios. However, the backscattering object (rear part of Saab) is a non-point scatter (explained in Section 4), which may present errors in the outcome. Therefore, based on the LOS measurements (blue data) in Figure 7a,b, it can be concluded that the backscattering signal correlates well with the FE, while the ground reflections cause the waving shape. Moreover, observation of the backscattering behaviour in the LOS conditions encouraged selecting WI software with its communication framework instead of alternative radar-oriented tools.

The measured results of the OLOS radar scenario with near-ground propagation is shown as red circles in Figure 7a,b. The obtained results show quite significant dispersion of the backscattering power over a wide range. However, linearisation with the least-squares method was applied to extract the proper mean values among the spread data (dashed black lines in Figure 7a,b). Specifically, if the antenna is installed at a height of $H = 0.3$ m, the mean excess loss is about 17 dB.
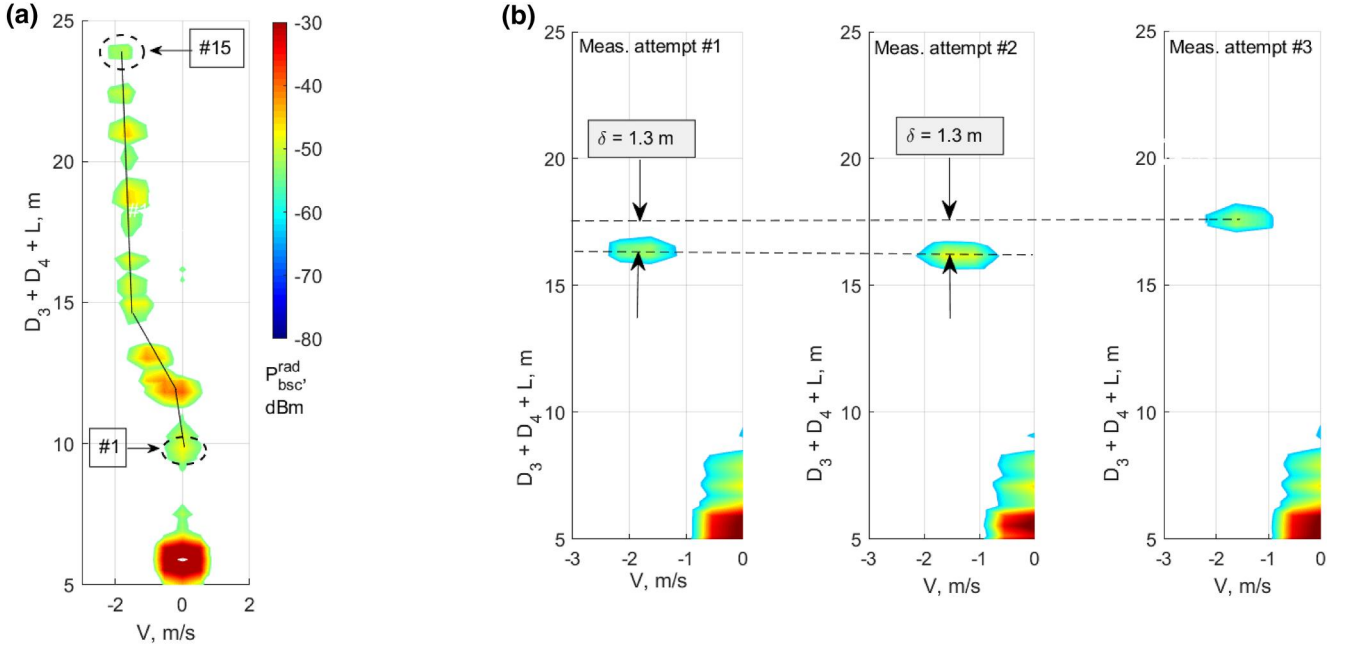
FIGURE 6 The measured backscattering power as a function of $D_3 + D_4 + L$ and speed: (a) 15 overlapped measured snapshots for a single driving. (b) Three measurement attempts of the same deployment to collect more statistics
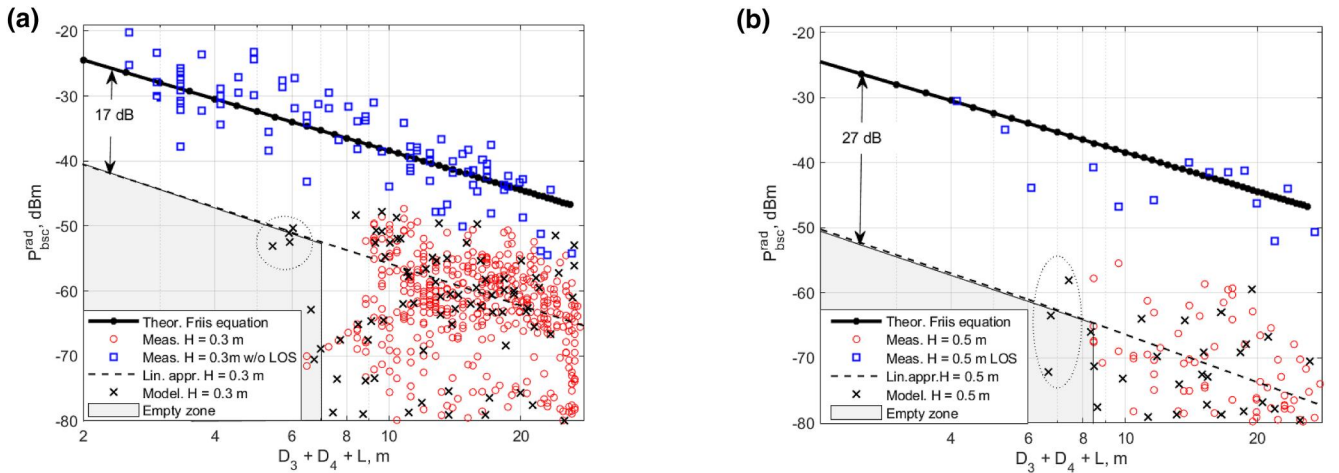

FIGURE 7 Measured (red circles) and modelled (black crosses) backscattering power as a function of $D_3 + D_4 + L$ at (a) $H = 0.3$ m and (b) at $H = 0.5$ m

Further increasing the height H to 0.5 m, decreases the average power by extra 10 dB.

The simulation results are presented as black crosses in Figure 7a,b. The simulation settings listed in Table 2 with a single reflection were utilised to obtain these figures. It can be seen that the general behaviour of the modelled data is well correlated with the measured one. However, several simulated values (circled in the figures) look suspicious. The same as communication simulation results, most likely, this mismatch relates to the physical method constraints and the limited accuracy of the 3D model. Also, the in-depth analysis of this effect is highly impeded due to the inability of the measuring setup to resolve highly dense multipath components travelling under the blocking vehicle.

5.3 | Sensitivity analysis in the communication deployment

Once the RT is calibrated based on the measurement results and provides a reasonable simulation accuracy, it can be reused for thorough study. Therefore, this section is dedicated to analysing the sensitivity of the total received power P_{tot}^{com} in the communication part. The scenario reveals the near-ground propagation picture to a greater extent than radar, with its chaotically spread data. Next, the cumulative distribution function (CDF) is chosen as a convenient method for statistical interpretation. Each simulated P_{tot}^{com} between Tx- and Rx-route components will serve as the reference data for the statistical analysis. Additionally, the summation of the multipath

components resulting in $P_{\text{tot}}^{\text{com}}$ is performed incoherently, that is, without dealing with the phase, to exclude an unnecessary multipath interference factor. Finally, the maximum limit of the multipath components has remained 50, and the simplified 3D model of Kia Ceed is reused as in previous sections.

Figure 8a exposes the CDF of the total received power as a function of the reflections limit. Specifically, the $P_{\text{tot}}^{\text{com}}$ was simulated for single, double and triple reflections limit (denoted as $1R$, $2R$ and $3R$ in Figure 8a) and for parameters listed in Table 2. In case of the single reflection (red lines in Figure 8a), the geometry of the dominant path is Tx-Road-Rx, while the alternative Tx-Car-Rx one is impossible for $H > a$ conditions thoroughly considered in this paper. At these settings, the total received power at 50% quantile is -51 dBm at $H = 0.5$ m and -47 dBm at $H = 0.3$ m. Next, at the double reflection limit settings (black lines in Figure 8a), the CDF repeats the shape of the one reflection limit due to the GO restriction—the path Tx-Road-Car-Rx is not feasible at $H > a$. This assumption might be additionally validated by the same number (400 pcs. vs. 400 pcs.) of obtained multipath components in the $1R$ and $2R$ modelling settings. Correspondingly, only the single reflecting paths contribute to the total received power $P_{\text{tot}}^{\text{com}}$ for these two cases.

When triple reflections and a single diffraction limit (blue lines in Figure 8a) are entered, the output modelling results change. Specifically, at 50% quantile, the total received power slightly rises up to -47 dBm and -46 dBm for $H = 0.5$ m and $H = 0.3$ m with respect to the $1R$ and $2R$ cases. In such conditions, the triple reflecting signal propagates along the Tx-Road-Car-Road-Rx geometrical path. Also, the $3R$ case brings additional 10 multipath components (400 pcs. in $1R$ and $2R$ vs. 410 pcs. in $3R$), captured by receivers at a closer distance D_2 than the $1R$ and $2R$ cases. Additional simulations discovered that the triple bouncing multipath component might create a high dense data cluster in the empty zone of Figure 5a,b at the distances 2–3 m less to the bounding line A. At the same time, the additional multipath components of the 3R limit setting may contribute to the total received

power. This is reflected in Figure 8a, where the CDF of the 3R case is shifted to the right.

The appearance of the dense clusters in the empty zones diverges with the measurement outcomes being carried out: the measured data is mostly located on the right-hand side from the bounding line A rather than in the grey zone. Therefore, the single reflecting multipath component (Tx-Road-Rx) most likely dominated in the measured results since no modelling-like data was captured, and no 'waveguide effect' was recognised. A detailed inspection of the Kia Ceed (see Figure 1a) bottom may confirm this statement since there are not so many (besides the gas tank) flat surfaces in the central part of the car, along which the signal should propagate. Accordingly, specular reflection cannot dominate in these conditions. However, the flat bottom shield might be attached to improve this adverse situation, especially to the central part with the silencer pipe. Fortunately, this under-body flattening has already been realised in commercial electric vehicles, where the flat battery enclosure is located at the very bottom. Such geometry is designed primarily due to the internal battery cell shapes, mass balance and aerodynamics.

As it has already been pointed out in Section 4, the invariance to the road surface conditions is the most remarkable property of the near-ground propagation. The travelling signal does not experience any dielectric or roughness losses due to grazing angle. Following this, the near-ground simulation of the communication deployment with a road roughness of 0.001 m was carried out at the $3R$ reflection limit setting. Other parameters are remained unchanged as in Table 2. This case was selected to maximise the interaction of the signal with the ground. The result of it is revealed in Figure 8a as a magenta curve. It is seen that the shape of the CDF distribution is almost identical to the case with zero roughness coefficient (blue curve). This behaviour entirely lives up to the expectations.

The next step is to demonstrate how the total received power $P_{\text{tot}}^{\text{com}}$ depends on the ground clearance. For this, the setting in Table 2 and single reflection parameter were
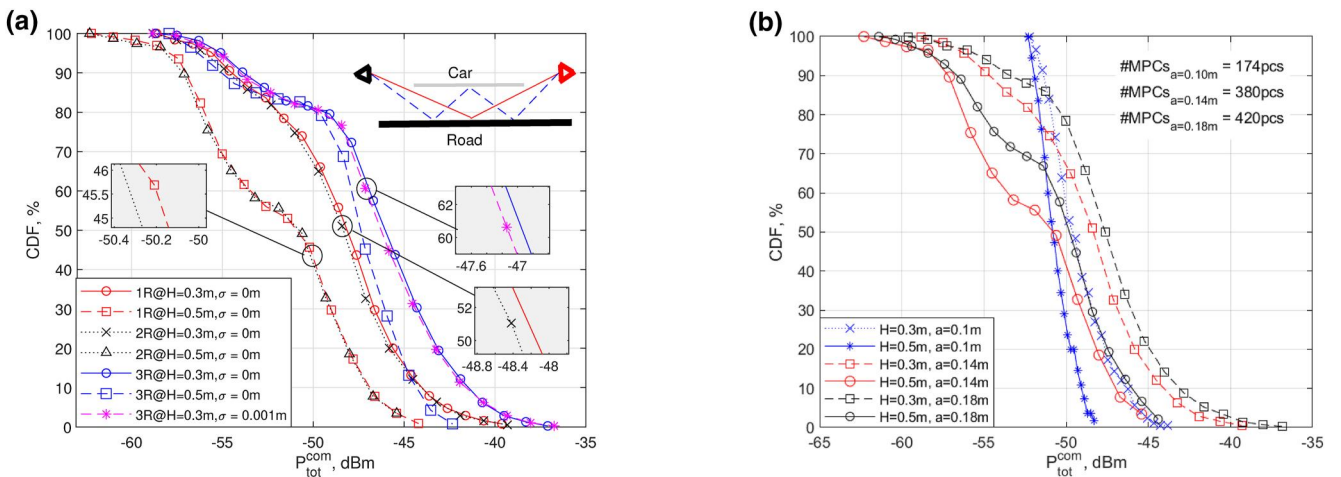

FIGURE 8 (a) CDF of the total received function as a function of the reflections limit. (b) CDF of the total received power as a function of the ground clearance

introduced. The result of this investigation is indicated in Figure 8b. Specifically, when the clearance is 0.1 m, the power is -50 dBm and -51 dBm at the 50% quantile for $H = 0.3$ m and $H = 0.5$ m. The distribution power range is relatively small and varies within 6–8 dBm. Further, rising the ground clearance to 0.14 and 0.18 m increase the total received power by weak 3 dB at $H = 0.3$ m and 50% quantile. On the contrary, the distribution power range enlarges to significant 20 dB. The reason why the average power remains almost the same at the 50% quantile, while the distribution spreads, can be justified with the multipath density and variability criteria. In particular, at the 0.1 m ground clearance, limited amount of propagation mechanisms exists at relatively large D_1 and D_2. Here, the road-car gap performs the keyhole effect [29], lessening the variability of the propagation mechanisms and characteristics. On the contrary, raising the ground clearance enhances the multipath variability and expands the range of D_1 and D_2, at which these multipath components become visible. This fact additionally can be approved by the number of arriving multipath components, shown in Figure 8b. Specifically, increasing the ground clearance from 0.1 to 0.18 m changes the number of multipath components from 174 to 420 pcs. As a result, a higher density of multipath components contributes to the total received power. Therefore, CDFs in Figure 8b are shifted along the X-axis proportionally to the number of arrived multipaths.

6 | CONCLUSION

This work completes the proof-of-concept study for the near-ground propagation for OLOS communication and automotive radar deployments. Future work includes measurements in real road conditions. The main contributions of this work can be summarised as follows:

1. The measured results were introduced, demonstrating the feasibility of the near-ground transmission in radar and communication V2V deployments.
2. The RT-based methodology was proposed and validated by the measurements.
3. The sensitivity analysis is completed, where the effect of the car geometry and road pavement was investigated.

First, the total received power and the back scattering power were measured at two antenna heights $H = 0.3$ and 0.5 m in the OLOS communication and radar deployment. The analysis of the communication part shows that at $H = 0.5$ m the blockage diminishing effect occurs at longer distances than when antennas are at $H = 0.3$ m. Specifically, the blockage-free near-ground propagation appears after $D_1 + D_2 + L = 10$ m at $H = 0.3$ m and after 20 m at $H = 0.5$ m. Next, after $D_1 + D_2 + L = 20$ m at $H = 0.3$ m and 24 m at $H = 0.5$ m, the captured total received power converges with the FE, due to the grazing incident and reflecting angle. The capability to detect the adjacent vehicles by radar via near-ground

propagation looks challenging due to significant losses at $H = 0.5$ m. In particular, at this height, the average losses relative to the Friis equation is 27 dB, while at $H = 0.3$ m, only 17 dB. Also, the first near-ground multipath were detected at $D_3 + D_4 + L = 6$ m for $H = 0.3$ m and 8 m for $H = 0.5$ m, accordingly.

The second stage, RT simulations, provides an intuitive picture of the near-ground propagation and might be effectively exploited for applied engineering problems. In this research work, the proposed RT-based methodology is validated by measurements. However, some modelled results are located far beyond the acceptable measured data range, which requires additional investigation in the future. This may happen due to the low accuracy of the employed 3D model or the limited RT methods for such complicated geometry.

Finally, the RT-based method was utilised to show the evolution of the total received power in communication scenario as a function of (i) reflection limit setting and (ii) ground clearance. Specifically, single- and double-reflections limit generate similar total received power distribution due to the impossibility of double-bouncing path geometry in the proposed scenario. Therefore, only single reflection in both cases contributes to the total received power. In its turn, the triple-reflection limit slightly increases the total received power, and reduces the D_1 and D_2 distances, at which the first near-ground multipath becomes detectable. The clearance lifting does not significantly (about < 3 dB) change the average total received power value, but it does affect the multipath variability and density. Higher the ground clearance, greater the number of propagation mechanisms and higher the density of the multipath components, travelling through the car-pavement gap.

CONFLICT OF INTEREST
The authors have declared no conflict of interest.

PERMISSION TO REPRODUCE MATERIALS FROM OTHER SOURCES
None.

DATA AVAILABILITY STATEMENT
No data are available.

ORCID
Dmitrii Solomitckii https://orcid.org/0000-0002-6143-393X

REFERENCES
1. Autonomous/Driverless Car Market - Growth, Trends, Covid-19 Impact, and Forecast (2021 - 2026). [Online]. https://www.reportlinker.com/p06101202/. Accessed 30 October 2021

2. Tesla Autopilot: US Opens Official Investigation Into Self-Driving Tech. [Online]. https://www.bbc.com/news/technology-58232137. Accessed 30 October 2021

3. Study on NR Vehicle to Everything (V2X) Services. Technical report, Release 16, 3GPP TR 38.885, Mar. 2019

4. Systems characteristics of automotive radars operating in the frequency band 76-81 GHz for intelligent transport systems applications, Rec. ITU-R M. 2057–2051 2018

5. Kumari, P., et al.: IEEE 802.11 ad-based radar: an approach to joint vehicular communication-radar system. IEEE Trans. Veh. Technol. 67(4), 3012–3027 (2017). https://doi.org/10.1109/tvt.2017.2774762

6. Tunc, C., Panwar, S.S.: Mitigating the impact of blockages in millimeter-wave vehicular networks through vehicular relays. IEEE OJITS. 2, 225–239 (2021). https://doi.org/10.1109/ojits.2021.3100856

7. Tunc, C., et al.: The blind side: latency challenges in millimeter wave networks for connected vehicle applications. IEEE Trans. Veh. Technol. 70(1), 529–542 (2020). https://doi.org/10.1109/tvt.2020.3046501

8. Solomitckii, D., et al.: Near-ground propagation measurements for vehicular deployments. In: 2021 15th European Conference on Antennas and Propagation (EuCAP), pp. 1–5 (2021)

9. Klaina, H., et al.: Characterization of near-ground radio propagation channel for wireless sensor network with application in smart agriculture. In: Multidisciplinary Digital Publishing Institute Proceedings. 2(3), 110 (2017). https://doi.org/10.3390/ecsa-4-04922

10. Meng, Y.S., Lee, Y.H., Ng, B.C.: Path loss modeling for near-ground VHF radio-wave propagation through forests with tree-canopy reflection effect. Prog. Electromagn. Res. 12, 131–141 (2010). https://doi.org/10.2528/pierm10040905

11. Klaina, H., et al.: Narrowband characterization of near-ground radio channel for wireless sensors networks at 5g-iot bands. Sensors. 18(8), 2428 (2018). https://doi.org/10.3390/s18082428

12. Hejselbæk, J., et al.: Empirical study of near ground propagation in forest terrain for internet-of-things type device-to-device communication. IEEE Access. 6, 54052–54063 (2018). https://doi.org/10.1109/access.2018.2871368

13. Joshi, G.G., et al.: Near-ground channel measurements over line-of-sight and forested paths. IEE Proc. Microw. Antenn. Propag. 152(6), 589–596 (2005). https://doi.org/10.1049/ip-map:20050013

14. Foran, R.A., Welch, T.B., Walker, M.J.: Very near ground radio frequency propagation measurements and analysis for military applications. In: MILCOM 1999. IEEE Military Communications. Conference Proceedings (Cat. No. 99CH36341). Vol. 1, pp. 336–340 (1999)

15. Li, Y., et al.: Research and experiment on UWB path loss characteristics in outdoor near-ground environments. Automat. Control Comput. Sci. 53(2), 186–193 (2019). https://doi.org/10.3103/s014641161902010x

16. Xu, C., et al.: Toward near-ground localization: modeling and applications for toa ranging error. IEEE Trans. Antenn. Propag. 65(10), 5658–5662 (2017). https://doi.org/10.1109/tap.2017.2742551

17. Duan, S., et al.: Ultra-wideband radio channel characteristics for near-ground swarm robots communication. IEEE Trans. Wireless Commun. 19(7), 4715–4726 (2020). https://doi.org/10.1109/twc.2020.2986446

18. Sangodoyin, S., Niranjayan, S., Molisch, A.F.: Ultrawideband near-ground outdoor propagation channel measurements and modeling. In: The 7th European Conference on Antennas and Propagation (EuCAP), pp. 3034–3038 (2013)

19. Sangodoyin, S., Niranjayan, S., Molisch, A.: A measurement-based model for outdoor near-ground ultrawideband channels. IEEE Trans. Antenn. Propag. 64(2), 740–751 (2015). https://doi.org/10.1109/tap.2015.2505004

20. Torabi, A., Zekavat, S.A.: A rigorous model for predicting the path loss in near-ground wireless sensor networks. In: 2015 IEEE 82nd Vehicular Technology Conference (VTC2015-Fall), pp. 1–5. IEEE (2015)

21. Automobile Dimensions: automobile dimensions and sizes of all makes. [Online]. https://www.automobiledimension.com/. Accessed 30 October 2021

22. Barneto, C.B., et al.: High-accuracy radio sensing in 5G new radio networks: prospects and self-interference challenge. In: The IEEE 53rd Asilomar Conference on Signals, Systems, and Computers, pp. 1159–1163 (2019)

23. Wireless InSite Offical Page. [Online]. https://www.remcom.com/wireless-insite-em-propagation-software. Accessed 30 October 2021

24. Balanis, C.A.: Antenna Theory: Analysis and Design. John wiley & sons (2015)

25. Knott, E.F., Schaeffer, J.F., Tulley, M.T.: Radar Cross Section. SciTech Publishing (2004)

26. Jaselskis, E.J., Grigas, J., Brilingas, A.: Dielectric properties of asphalt pavement. J. Mater. Civ. Eng. 15(5), 427–434 (2003). https://doi.org/10.1061/(asce)0899-1561(2003)15:5(427)

27. Wireless InSite features. [Online]. https://www.remcom.com/wireless-insite-em-propagation-software-wireless-insite-em-propagation-features/. Accessed: 30 October 2021

28. Solomitckii, D., et al.: Characterizing radio wave propagation in urban street canyon with vehicular blockage at 28 GHz. IEEE Trans. Veh. Technol. 69(2), 1227–1236 (2020). https://doi.org/10.1109/tvt.2019.2959127

29. Almers, P., Tufvesson, F., Molisch, A.F.: Measurement of keyhole effect in a wireless multiple-input multiple-output (mimo) channel. IEEE Commun. Lett. 7(8), 373–375 (2003). https://doi.org/10.1109/lcomm.2003.815655